A numerical simulation study of the collisional-interchange instability seeded by the pre-reversal vertical drift

Jonas Sousasantos,[1] E. A. Kherani,[1] and J. H. A. Sobral[1]

[1] The collisional interchange instability (CII) is known to lead to the equatorial plasma bubble (EPB) development when the ionosphere is raised to higher altitudes by the prereversal electric field or vertical drift (PRVD). The PRVD presents considerable longitudinal variation (with scale size $\sim 15°$) across the sunset terminator and this variation may act as a seeding perturbation as proposed by Woodman (1994) and Huang and Kelley (1996b). In the present work, we examine the efficiency of this longitudinal variation of the PRVD to act as a seeding for the CII and to give rise to EPB in the absence of any other kind of initial perturbation. To do so, we carried out the CII simulation at the equator in a plane perpendicular to the magnetic field. We consider a few simplified cases choosing a Gaussian-shaped longitudinal variation of PRVD with various possible minimum and peak values and finally consider a realistic case with a spatial-temporal configuration of PRVD obtained using SAMI2 model. Simulations with simplified cases show that the EPB develops only for minimum value greater than 20 m/s and amplitude (difference between the peak-to-minimum value) greater than 40 m/s. Simulation with a realistic case shows that the PRVD during high solar flux summer satisfies these threshold conditions and with the seeding scale $\sim 15°$, the EPB of longitudinal size $\approx 2°$ is developed toward east of the PRVD peak.

1. Introduction

[2] The collisional interchange instability (CII) which is the generic term for the Gradient-drift, ExB, and Gravitational Rayleigh-Taylor instabilities, is believed to play a crucial role in the onset and development of equatorial spread F turbulence [*Haerendel*, 1973]. Radar observations of the equatorial spread F reveal the existence of plumes that may penetrate to the topside F layer attaining very high altitudes [*Woodman and LaHoz*, 1976]. These plumes are identified as large-scale depletions or equatorial plasma bubbles (EPB) [*Sobral et al.*, 1980] and are believed to be generated by CII mechanism [*Sultan*, 1996]. Numerous theoretical and numerical studies have been performed to assess the linear and nonlinear aspects of these complex processes [*Ossakow et al.*, 1979; *Zargham and Seyler*, 1987; *Raghavarao et al.*, 1992; *Huang et al.*, 1993; *Keskinen et al.*, 1998]. These studies revealed the generation of the EPB initiated by a seed perturbation at the bottomside of the rising F layer. The seed perturbation used is either in the form of plasma density perturbation [*Kherani et al.*, 2004; *Huba and Joyce*, 2007] or of

wind perturbation [*Huang and Kelley*, 1996a; *Kherani et al.*, 2009; *Keskinen*, 2010]. The seed perturbation may also arise from the shear instability as shown by *Aveiro et al.* [2011].

[3] The prereversal-vertical-drift (PRVD) contributes to the growth of CII (here CII is referred to the Generalized Rayleigh-Taylor instability that excludes the Gradient-drift instability) in two ways: first, it accelerates the growth rate of ExB instability in the bottomside of the F region, and second, it accelerates the growth of Gravitational Rayleigh-Taylor instability by elevating the bottomside to the higher altitude [*Ossakow et al.*, 1979; *Sekar et al.*, 1994]. Both contributions are decisive for the formation of the EPB. Various observations indicate that the PRVD acquires considerable longitudinal variation across the sunset terminator such that it peaks at the location toward the nightside of the sunset terminator and decreases both toward east and west of this location [*Balsley*, 1973; *Fejer et al.*, 1991, 2012; *Batista et al.*, 1986, 1996]. According to *Huang and Kelley* [1996b], this longitudinal feature can be modeled as a quasi-Gaussian electric field or vertical drift with pulse width about 2000 km full width at half maximum which also travels westward with the terminator. For example, during very high (high) solar flux period, F10.7 > 200 (F10.7 $\sim$ 200), the PRVD typically varies as a quasi-Gaussian shape with minimum 20 m/s to maximum 60 m/s within 1 h (1.5 h) effectively corresponds to approximately 1500 km (2000 km) longitudinal scale across the terminator [*Fejer et al.*, 1991; *Abdu et al.*, 2010].

[1]DAE-INPE, São Jose dos Campos, São Paulo, Brazil.

Corresponding author: J. Sousasantos, DAE-INPE, 12227-010, São Jose dos Campos, SP, Brazil. (jonas.sousa@dae.inpe.br)

[4] Simulation studies so far considered the PRVD as an ambient time-varying parameter, leading to the rapid growth of CII in the presence of a seeding perturbation. This seed perturbation is defined as the longitudinal wave-like variation with the scale size ∼50–500 km, and over this scale, the PRVD is usually considered to be longitudinally invariant which is indeed the case. However, another interesting aspect concerning seeding mechanism was proposed by *Woodman* [1994] and *Huang and Kelley* [1996b]. *Woodman* [1994] proposed that the longitudinal-varying PRVD could itself act as a seed perturbation for the development of the EPB while at the same time contributing directly to the growth of CII. *Huang and Kelley* [1996b] presented a conceptual sketch (Figure 2 in their paper) showing the formation of a EPB with the seeding from the longitudinal-varying PRVD as proposed by *Woodman* [1994]. This proposal is the motivation of the present study. In the present work, using two dimensional simulation model of CII, we examine the efficiency of a longitudinally varying PRVD with very large scale to seed the CII and to give rise the EPB development by considering a few simplified cases and finally a realistic case. In these simplified cases, we consider the Gaussian-shaped PRVD with the scale size equal to 1500 km covering the longitude region from evening to nighttime corresponding to about 1 h local time variation during prereversal phase. In a realistic case, we consider the spatial-temporal configuration of the PRVD obtained using SAMI2 model [*Huba et al.*, 2000].

2. Model Equations and Algorithms

[5] We adopt, here, the following set of equations to study the CII in the equatorial F region [*Kherani et al.*, 2004]:

$$\frac{\partial n}{\partial t} + \vec{\nabla} \cdot (n\vec{u}_e) = -\beta n - \alpha n^2 \qquad (1)$$

$$\vec{\nabla} \cdot \vec{J} = e\vec{\nabla} \cdot [n(\vec{u}_i - \vec{u}_e)] = 0. \qquad (2)$$

$$\vec{u}_{i,e} = \frac{\kappa_{i,e}}{1 + \kappa_{i,e}^2} \vec{v}_{i,e} \times \hat{b} + \frac{1}{1 + \kappa_{i,e}^2} \vec{v}_{i,e} \qquad (3)$$

where

$$\vec{v}_{i,e} = \frac{-c_{si,e}^2}{\nu_{i,en}} \vec{\nabla} \log n + \frac{\vec{g}}{\nu_{i,en}} + b_{i,e}(\vec{E} + \vec{W} \times \vec{B}_o) + \vec{W}$$

[6] The subscripts "*e*" and "*i*" refer to the electrons and ions, respectively. Equations (1) and (2) are the ion continuity and divergence free current ($\vec{J}$) equations, respectively, while $\vec{u}_{i,e}$ in equation (3) are the ion and electron's velocities obtained by neglecting the inertial dynamics as compared to the collisional dynamics in the corresponding momentum equations. The plasma is assumed to be charge neutral ($n_e = n_i = n$), and it is ensured by (2). The terms in the right-hand side of (1) correspond to the chemical loss of electrons by charge exchange process (β) and dissociative recombination process (α), respectively. The notations $\kappa_{i,e}$ represent the ratios of the gyrofrequencies, $\Omega_{i,e}$, to collision frequencies, $\nu_{i,en}$ of the corresponding species, $b_{i,e} = e/m_{i,e}\nu_{i,en}$ represent the corresponding mobilities, $\vec{E}$ is the electric field in the neutral wind ($\vec{W}$) frame, $\hat{b}$ is the unit vector in the magnetic field, $\vec{B}_o$, direction and $c_{si,e}$ are the ions and electrons thermal

velocities, respectively. For further analysis, the thermal effects, i.e., diffusion effects, are neglected restricting our investigation to be applicable only for large scales. The diffusion effects are important to study the saturated turbulent state of the instability [*Keskinen et al.*, 2003]. However, in the present investigation, the nonlinear evolution of the CII rather than the saturated turbulent is investigated. Also neglected are the ion-inertia effects and dynamics parallel to the magnetic field. The inertia effects are important above 600 km, and thus, the present simulation is applicable below 600 km altitude. The dynamics parallel to the magnetic field is ignored and local values of ionospheric parameters, instead of field-line-integrated, are used. This is limitation of the present study which will exclude the studies concerning the effects of off-equatorial dynamics on the evolution of EPB.

[7] The chemical loss-production effects are retained in the present study via effective recombination rate R_e defined below. Equations (1)–(3) are solved at the magnetic equator in the Cartesian coordinate system where $\hat{x}$, $\hat{y}$, and $\hat{z}$ correspond to the westward, upward, and Earth's magnetic field directions, respectively. For a realistic case, equations (1)–(3) are solved in the magnetic field coordinate system (ϕ, p) at the equator where ϕ, p represent the longitude and altitude, respectively. This coordinate system is adopted since the SAMI2 model uses this system and outputs of this model is used as the inputs to the CII model for a realistic case in the present study. Assuming a electrostatic perturbation ($\delta\vec{E} = -\vec{\nabla}\Phi$) of the electric field $\vec{E} = \vec{E}_o + \delta\vec{E} = \vec{E}_o - \vec{\nabla}\Phi$, the total current density $\vec{J}$, which is the sum of the steady state and the perturbed current density, is obtained, as equation (A1) in Appendix A. Substitution of this current density into the divergence-free current density equation (2) leads to the following equation for the perturbed potential (Φ) in the F region, derived as (A2) in Appendix A:

$$\nabla \cdot (\sigma_P \nabla \Phi) = B_o \Delta u^o \cdot \nabla \sigma_P \qquad (4)$$

The ion continuity equation (1) can be written as follows:

$$\frac{\partial n}{\partial t} + \vec{F}(n, \Phi) \cdot \vec{\nabla} \log n = R_e n \qquad (5)$$

where

$$R_e = \left(\frac{1}{\beta} + \frac{1}{\alpha n(t)}\right)^{-1}$$

is the effective recombination rate and

$$\vec{F} = n(u_{yt}\hat{y} + u_{ox}\hat{x} + \delta\vec{u}); \quad \vec{u}_{yt}(\vec{x}, t) = u_o(t)u_y(\vec{x})\hat{y}; \quad \delta\vec{u} = -\left(\frac{\vec{\nabla}\Phi}{B_o}\right) \times \hat{b}_o \qquad (6)$$

is the particle flux. Here u_{yt} represents the ambient PRVD, composed of the time, $u_o(t)$, and longitudinal, $u_y(x)$, varying components. In the present work, u_{yt} acts as a seeding perturbation owing to the longitudinally varying u_y term. u_{ox} represents the zonal drift of ionosphere associated with the zonal shear flow as a result of the thermospheric eastward wind during evening-nighttime. The zonal shear flow leads to the generation of confined bottomside bubble as shown by *Sekar and Kelley* [1998] and *de Paula et al.* [2011]. It also leads to the generation of the shear instability which then combines with the CII to generate the bottomside
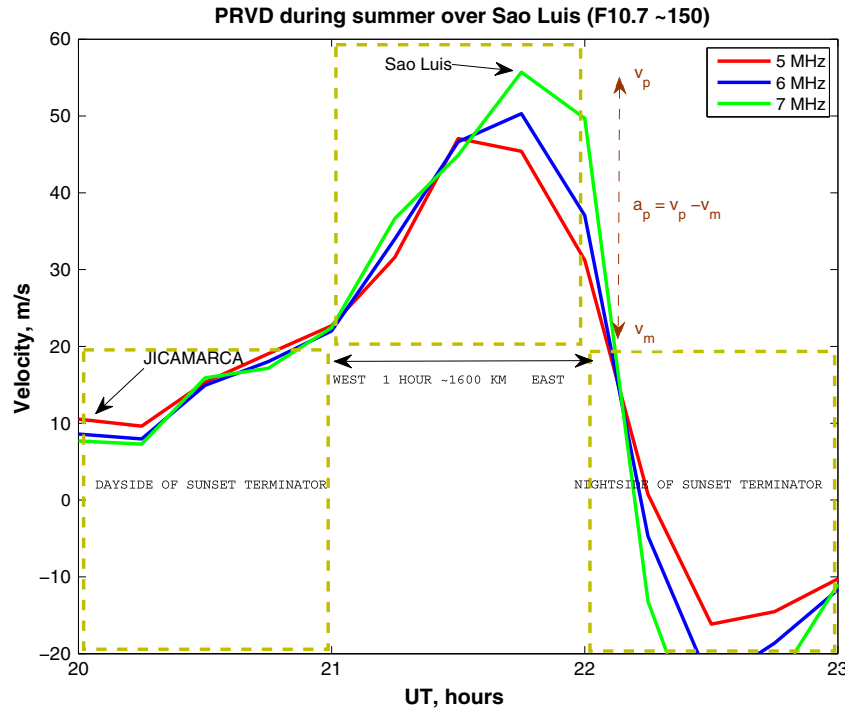
Figure 1. Definition of longitudinal-varying PRVD: PRVD deduced from São Luís digisonde during December 2002 (high solar flux) is shown.

bubble as shown theoretically by *Hysell et al.* [2005], *Kudeki et al.* [2008], and *Aveiro et al.* [2011] and experimentally by *Rodrigues et al.* [2008]. The effects of the zonal shear flow is not considered in the present work, and u_{ox} is taken to be zero. In equation (6), $\delta \bar{u}$ represents the perturbed ion velocity in the F region and is mainly due to the dominant Hall mobility.

[8] Equations (4)–(6) form a coupled closed system of equations for the CII in the F region. With a chosen u_{yt} and the ambient ionospheric conditions (as described below and in Figures 1-2, 5), the continuity equation (5) is solved using Crank-Nicolson an implicit scheme at first [*Kherani et al.*, 2004]. The potential equation (4) is then solved using Successive-Over-Relaxation algorithm with the perturbed density. This solution is again substituted into (5) to obtain a time-evolving density, and this loop continues until the ions maximum upward velocity becomes 500 ms^{-1}. The finite difference equations corresponding to the differential equations (4) and (5) are derived in Appendix B. Under simplified cases, equations (4)–(6) are solved in Cartesian coordinates (x, y) at the equator where x and y represent the longitude and altitude, respectively. The x-boundaries are located at 0 and 1500 km with the grid resolution $\Delta x = 10$ km. The y-boundaries are located at 150 km and 600 km with the grid resolution $\Delta y = 5$ km. For the realistic case, equations (4)–(6) are solved in the magnetic field coordinates (ϕ, p) at the equator where ϕ and p represent the longitude and altitude, respectively. The ϕ-boundaries are located at 332° and 302° with grid resolution $\Delta \phi = tan^{-1}(\Delta x/(R_e + 300))$ where R_e is the Earth's radius and $\Delta x = 10$ km. The p-boundaries are located at 150 km and 600 km with a grid resolution $\Delta p = \Delta y = 5$ km. The transmittive boundary condition on n and the Neumann

boundary condition on Φ are imposed on these boundaries. These boundary conditions are the same as those chosen by *Kherani et al.* [2004] and sufficient to ensure the vanishing current density across the lower boundary provided that the ambient ionosphere is invariant at the boundary.

3. Nature of u_{yt}

[9] In Figure 1, PRVD, u_{yt}, over São Luís equatorial station during high solar flux (F10.7 $\sim$ 150–200) summer season is depicted. Considering that São Luís is at a longitude where the peak PRVD occurs between 21:30 and 21:45 UT, a longitudinal region around this location can be constructed that covers evening-to-night (21:00–22:00 UT) or the sunset terminator corresponding to the scale size of approximately 1500 km. Outside this zonal region, toward west, the ionosphere is still in the dayside and cannot be included in the present simulation of CII. It is evident from this figure that within the zonal region covering the sunset terminator, the PRVD varies from the minimum value (v_m) of 20 m/s to the peak value (v_p) of $\sim$ 50–55 m/s within 1500 km zonal distance. Here, we can characterize the PRVD with the peak value (v_p), the minimum value (v_m), and the amplitude ($a_p = v_p - v_m$). Thus, by these definitions, the PRVD acquires the amplitude (a_p) of 30–35 m/s with the peak value (v_p) of $\sim$ 50–55 m/s and scale size of $\sim$ 1500 km. During very high solar flux (F10.7 > 200), v_p, v_m, and a_p may exceed the values shown in Figure 1 as reported by *Fejer et al.* [1991] and *Abdu et al.* [2010].

[10] We have chosen $u_{yt}(x, t) = u_o(t)u_y(x)$ as written in equation (6), where $u_o(t)$ and $u_y(x)$ represent the temporal and longitudinal variations. It is clear from Figure 1 and SAMI2 simulation results (shown later in Figure 5) that
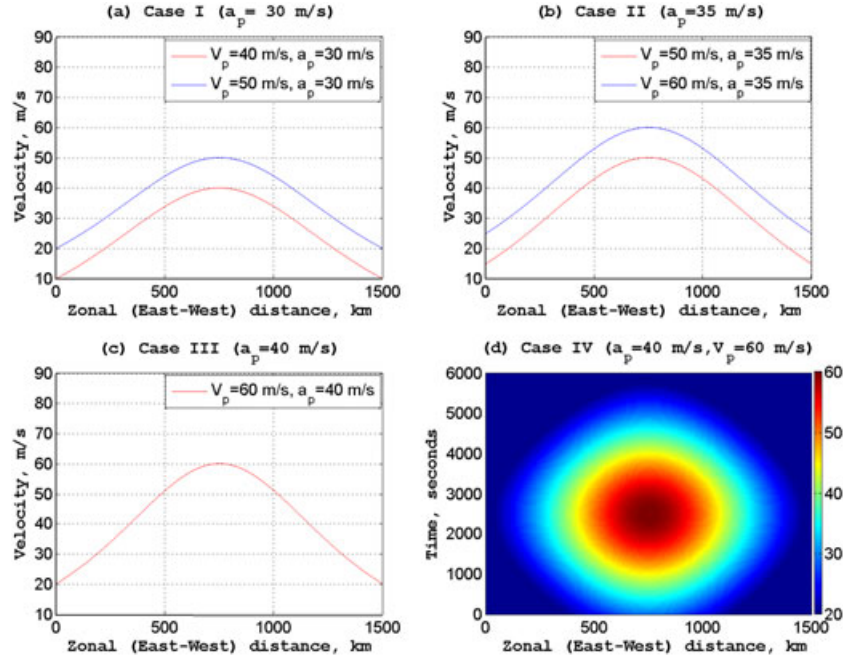
Figure 2. (a–c) Various longitudinal configurations of the PRVD under Cases I–III, respectively, where $u_o(t) = 30$ m/s is considered. (d) Longitudinal-time variation of PRVD under Case IV with $u_{ox} = 0$ (i.e, the sunset terminator is kept fixed).

both $u_o(t)$ and $u_y(x)$ vary as quasi-Gaussian in time and longitude, respectively. In order to understand the effects of temporal and longitudinal variation separately, we first begin with the time averaged value of $u_o(t)$ under Cases I–III; i.e., the PRVD profile, $u_{yt}(x, t)$, is just a function of the longitude x. We have taken the time averaged value equal to 30 m/s since during 21:00–22:00 UT, the PRVD varies between 20 and 60 m/s but remains between 20 and 40 m/s for most of the time during this time interval. Cases I–III examine the effects of various configurations of $u_y(x)$, based on different values of parameters a_p and v_p as follows:

[11] Case Ia: $a_p = 30$ m/s, $v_p = 40$ m/s; Case Ib: $a_p = 30$ m/s, $v_p = 50$ m/s

[12] Case IIa: $a_p = 35$ m/s, $v_p = 50$ m/s; Case IIb: $a_p = 35$ m/s, $v_p = 60$ m/s

[13] Case III: $a_p = 40$ m/s, $v_p = 60$ m/s

[14] In all these configurations, the longitudinal varying component, $u_y(x)$, of u_{yt} is chosen to be the Gaussian with a 1500 km base width (full width at the minimum value). Moreover, these profiles remain fixed in the longitude; i.e., the movement of the sunset terminator is not considered. These profiles are shown in Figures 2a–2c.

[15] In the next simulation run referred as Case IV, we choose the longitudinal configuration, $u_y(x)$, corresponding to Case III but consider a quasi-Gaussian variation of $u_o(t)$ in time in equation (6), instead of a time-averaged $u_o(t)$. The longitudinal-time variation of $u_{yt}(x, t)$ for this case is shown in Figure 2d.

[16] In the final simulation run referred as a realistic case, Case V, the spatial-temporal configuration of the ambient PRVD is obtained using SAMI2 model [*Huba et al.*, 2000]. This case represents the realistic case where the spatial-temporal variations of the PRVD and density that also include the effects of the movement of the sunset terminator are obtained using SAMI2 model.

[17] In general, the PRVD increases with altitude below the height of the F-peak, as reported by *Fejer et al.* [1991] also evident from Figure 1. In the present work, the altitude-average PRVD, u_{yt}, is considered; i.e, u_{yt} does not depend on y.

4. Results and Discussion

4.1. Simplified PRVD Configuration: Cases I–IV

[18] The simulation results corresponding to Cases I–IV are shown in Figures 3-4. To infer the development of EPB under the action of CII for simplified cases, we monitor the time history of the maximum vertical velocity (v_{max}, the vertical component of $\delta\vec{u}$) inside the density depletion. The linear, exponential, and multiexponential growth of this velocity with time represent, respectively, the steady state, linear growth, and nonlinear growth (or the development of the EPB) of CII [*Kherani et al.*, 2009].

[19] Figure 3 depicts the time variation of v_{max} for Cases I–IV, respectively. In these plots, also plotted (green curve) is the time variation of the PRVD, $u_o(t)$, which is constant for Cases I–III and varying in time for Case IV. It is evident from Figure 3a that v_{max} remains constant with time for Case Ia suggesting that the EPB does not develop under Case Ia. The EPB does not develop for Case IIa also as evident from Figure 3b. On the other hand, for Cases Ib, IIb, and III, v_{max} increases linearly initially for 7000 s and then increases exponentially and then multiexponentially in 8000 s. Such growth suggests the EPB development under these cases.
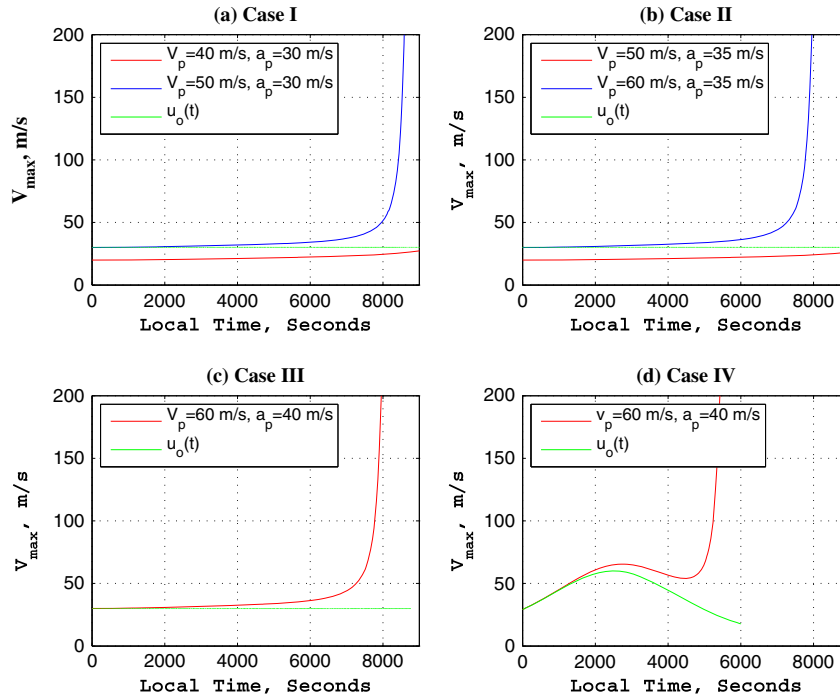
Figure 3. The time variation of the maximum upward velocity inside a depletion for (a) Case I, (b) Case II, (c) Case III, and (d) Case IV. In all these plots, the green curve represents the time variation of PRVD, $u_o(t)$, and it is equal to 30 m/s for Cases I–III and time varying for Case IV.

[20] The EPB does not develop for small peak ($v_p =$ 40 m/s) value under Case Ia when a_p equals to 30 m/s. However, for the same a_p, the EPB develops under Case Ib when v_p is raised to 50 m/s. The different characteristics between Ia and Ib suggests the importance of large value of v_p to support the development of the EPB.

[21] It is then interesting to note that the EPB does not develop for Case IIa which has $a_p = 35$ m/s larger than Case Ib and has same v_p value as Case Ib. In spite of a large a_p in Case IIa as compared to Case Ib, the EPB does not develop for Case IIa since the base value or minimum value v_m for this case is lower than 20 m/s similar to the nondeveloped
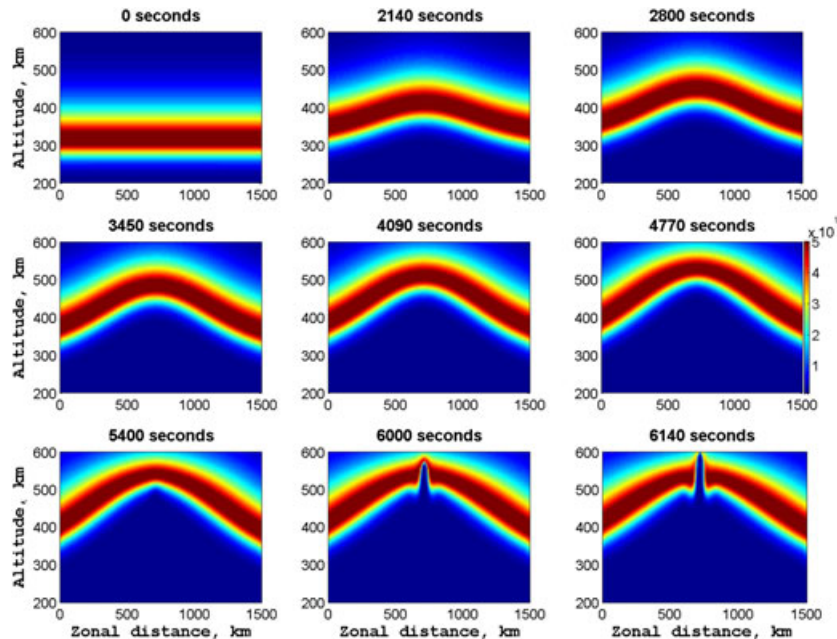
Figure 4. Case IV: Isodensity contours (represented by pixmap) in altitude-longitude plane at different time of evolution of EPB.

Case Ia. This suggests that in addition to a large value of v_p, the value of v_m larger than 20 m/s is essential for the EPB development.

[22] For further study under Case IV, we choose the zonal configuration corresponding to the developed Case III, when the EPB develops within 8000 s, faster than other two developed Cases Ib and IIb. The time evolution of v_{max} for Case IV is plotted in Figure 3d. It is evident that for Case IV, the EPB develops within 5500 s, much faster than it develops under Case III. The EPB development in 5500 s is approximately the time duration of PRVD in the ionosphere represented by the green curve in Figure 3d. This situation represents the favorable condition for the EPB development. On the other hand, for 50 m/s $< v_p <$ 60 m/s, 30 m/s$< a_p <$ 40 m/s, the EPB may develop for $v_m >$ 20 m/s as in Cases Ib, IIb, and III. However, this development occurs in 8000 s, much later than usual time duration of PRVD in the ionosphere, and thus does not represent the favorable conditions for the EPB development. It should be noted that in spite of having the same Gaussian envelope of PRVD under Case III and Case IV, the CII grows much faster under Case IV. The possible reason is the different nature of $u_o(t)$ which in Case III is 30 m/s while in Case IV varies from 20 m/s to 60 m/s such that it remains larger than 30 m/s during 500–5000 s. In other words, the effectively larger $u_o(t)$ led to the faster growth of CII under Case IV.

[23] In Figure 4, the temporal evolution of the isodensity contours in the longitude-altitude plane are plotted for Case IV. Each panel in this figure corresponds to a time (denoted in the top of the panel) during the evolution of CII. It is evident that for the first 5000 s, the longitudinal variation of the PRVD leads to the differential uplift of ionosphere leading to the formation of the huge depletion. As the time progresses, the uplift around the PRVD peak location becomes larger and eventually develops as an EPB under the action of CII. It is to be noted that the entire $\sim$ 1500 km longitudinal scale does not participate in the EPB development. It is the scale of order of $\sim$ 100 km located around the PRVD peak at $x =$ 750 km that develops into EPB. Therefore, effect of extremely large scale seeding is to not create a huge bubble of similar size but to develop as a bubble of size of order of $\sim$ 100 km. The seeding mechanism proposed by *Huang and Kelley* [1996b] is as follows: Initially, large longitudinal variation of PRVD leads to the huge depletion owing to the uplift of ambient ionosphere. The part of this huge depletion which is uplifted to the altitude above 500 km will then become the EPB of 300–400 km scale under the action the CII. The characteristics noted in Figure 4 are consistent with this proposed mechanism.

[24] In the present work, the seeding scale size is equal to 1500 km which is extremely large as compared to the seeding perturbation wavelengths ($\sim$50–500 km) usually considered in the previous simulation studies. It is, however, to note that the required amplitude (velocity perturbation) of seeding in the present study is a_p which is 40 m/s under Case IV. This initial amplitude is much larger than the velocity perturbation ($\sim$5 m/s) caused by the initial density or gravity wave perturbations. Thus, though seeding scale is extremely large in the present study, if the amplitude of this seeding is sufficiently large, as under Case IV, the large seeding scale may still give rise to the EPB development. We also note from no plasma bubble development Cases Ia and

IIa that such extremely large scale is sensitive to the amplitude and even for amplitude as large as 30 m/s, the EPB does not develop under Cases Ia and IIa. Thus, the spatial scale associated with the PRVD imposes the extreme condition for the EPB development.

4.2. CII Simulation With Realistic Ionospheric Dynamics Obtained Using SAMI2 Model

[25] Cases I–IV represent oversimplified ionospheric conditions where the configuration of the PRVD is kept fixed in space and the movement of the sunset terminator is not considered. However, these choices are not arbitrary but based on Figure 1 and SAMI2 simulation since either longitudinal or temporal or both variations are considered to be the quasi-Gaussian. In general, $u_{yt}(x, t)$ is a complex function of the longitude, time, and the movement of the sunset terminator. Therefore, to examine the effects of these variables (except the movement of the sunset terminator) separately, a few simplified Cases I–IV are examined first. Cases I–III are chosen to understand the effects of v_m, a_p and the quasi-Gaussian nature of the longitude dependence of $u_{yt}(x, t)$. Having known these effects, we then examined the Case IV where we introduced the quasi-Gaussian variation in time, instead of taking the time-averaged value of $u_o(t)$. The studies under Cases I–IV clearly suggested that the large values of v_m, a_p and the narrow quasi-Gaussian envelope are suitable for the seeding of the EPB. Based on these information, we search for a realistic u_{yt} during high solar flux when v_m, a_p are expected to be large and the quasi-Gaussian envelope in the longitudinal is expected to be narrow. Having studied the effects of these parameters/variations separately under the Cases I–IV, we may now examine the CII evolution under a realistic Case V where all these variations, including the movement of the sunset terminator, are considered together.

[26] In order to study the mechanism of PRVD seeding under realistic ionospheric conditions, we obtain the spatial-temporal configuration of the PRVD, $u_{yt}(x, t)$ and the ambient electron number density (or ionospheric density) n_o, using SAMI2 model for December month with F10.7=200 and zero neutral wind [*Huba et al.*, 2000]. SAMI2 is an ambient ionospheric model in two dimensions consisting of latitude-altitude plane. For our purpose, we extend SAMI2 model to three dimensions by adding a loop for the longitude and acquire the longitudinal-temporal configuration of the PRVD. Moreover, in order to obtain a well adopted profile of n_o which is the solution of the continuity equation in SAMI2, the model is run for 48 h. In Figure 5a, the longitudinal-temporal variation of the PRVD (represented by pixmap, i.e., 2D color plot) and the bottomside ionospheric density n^b (represented by black-contours) are shown for the time interval of 20:00–22:30 UT and in the longitude region covering 335–305°. The n^b represents the average electron number density in the altitude range of 250–450 km. In Figure 5b, the longitude-altitude profile of the ionospheric density n_o, at 21:40 UT is shown. We note the following characteristics from 5a:

[27] 1. At a given time, the PRVD reveals an asymmetric quasi-Gaussian variation with longitudes such that the vertical velocity decreased from peak value equal to 65 m/s to 20 m/s within 5° toward east and within 10° toward west.

[28] 2. At a given time, the n^b also reveals the asymmetric quasi-Gaussian variation with longitudes such that
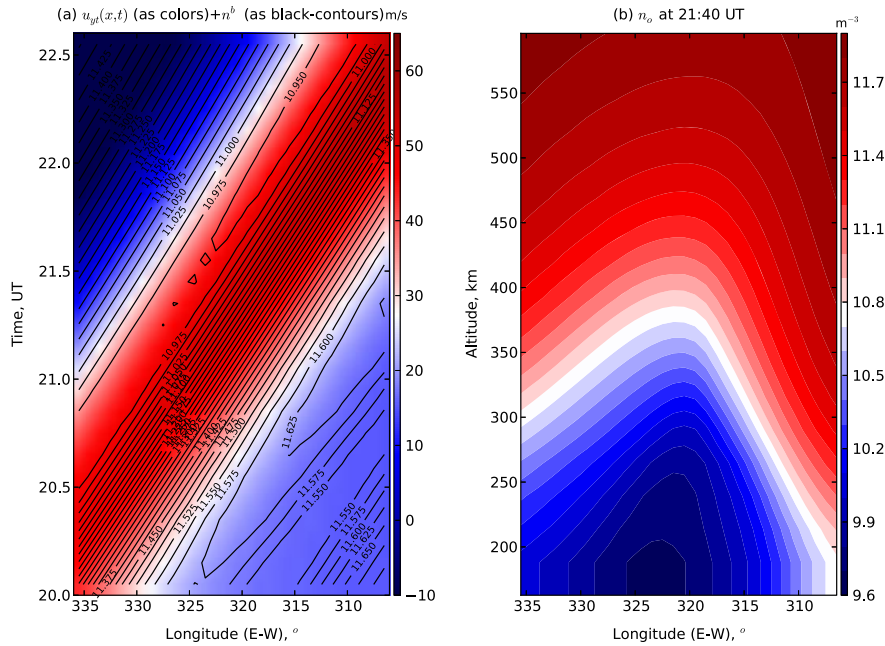
Figure 5. Ambient ionospheric conditions using SAMI2 model for F10.7=200 during December months: (a) the spatial-temporal configuration of PRVD, $u_{yt}(x, t)$ (represented by pixmap with scale represented by colorbar), and the bottomside number density n^b (represented by black contours, in log-scale). (b) The longitude-altitude configuration of the ambient electron number density n_o (in log-scale) at 21:40 UT.

this quasi-Gaussian envelope is collocated with the quasi-Gaussian envelope of the PRVD.

[29] 3. At a given time, the longitudinal extent of these quasi-Gaussian envelopes are of the order of 15°.

[30] 4. With time, these envelopes of the PRVD and n^b move westward (with velocity equals to the sunset terminator velocity) such that the both envelopes are locked together.

[31] 5. Figure 5b reveals the presence of quasi-Gaussian longitudinal variations in the ionospheric density, n, that is more pronounced in the bottomside altitude region (250–450 km). This quasi-Gaussian density envelope results from the quasi-Gaussian envelope of the PRVD, and it suggests the availability of the quasi-Gaussian seeding in the bottomside of the equatorial F region.

[32] These aspects imply that both quasi-Gaussian envelopes of PRVD and n^b (or n_o) are locked with the sunset terminator, moving together in time. This means that during the main phase of the pre-reversal, the seeding from PRVD always acts in the ionospheric region which is moving together with the quasi-Gaussian envelope of the PRVD. Therefore, it is expected that the seeding from PRVD should be coherent in time and very effective owing to the synchronized movement of the ionosphere and PRVD with the sunset terminator.

[33] Under a realistic Case V, the CII simulation begins at $t = t_o = 18 : 30$ UT and PRVD configuration shown in Figure 5a is used for $u_{yt}(x, t)$ in the CII simulation to run under the realistic ionospheric conditions. The initial density profile is not directly taken from SAMI2. However, it is chosen such that it has the bottomside density gradient and the peak density height consistent with the high solar flux summer season density profile obtained from SAMI2.

The initial density at $t = 18 : 30$ UT is chosen to be invariant in the longitude, and for the next 3 h, the simulation is run so that the longitudinal variation in the density is self-consistently developed by the u_{yt} and leads to the density modulation similar to the SAMI2 during 20:00 UT–21:40 UT. The interval 20:00 UT–21:40 UT is chosen since during this time interval, the PRVD begins to enter from east to the simulation box (335°–305°) and remains in the evening prereversal phase, as may be noted from Figure 5a. Moreover, as evident from Figure 5b, at $t = 21 : 40$ UT, the density acquires the longitudinal variation that may efficiently seed the CII.

[34] In Figure 6, the evolution of the ambient PRVD (represented by pixmap) and the iso-density-contours (represented by colored-contours) over longitude-altitude plane are shown for few chosen time (mentioned at the top of each panels). We note that during 20:00–21:40 UT, the ionospheric density, n_o, acquires a quasi-Gaussian envelope in the longitude owing to the quasi-Gaussian envelope of the PRVD. The quasi-Gaussian envelope at $t = 21 : 40$ UT is characterized by a peak located near longitude equal to 322° that covers 330–315° longitudes. This envelope is similar to the quasi-Gaussian envelope obtained using SAMI2 model, as shown in Figure 5b. However, we may also note that this envelope has slightly less altitude modulation than the envelope in Figure 5b. This may be owing to the constant altitude profile of u_{yt} as considered in the present study, which otherwise should increase with altitude as considered in the SAMI2 model. Moreover, the longitudinal variation in the production rate, which is not considered in the present study while considered in the SAMI2 model, may also contribute to cause the noted differences. However, it is obvious that if the slightly lesser altitude modulated envelope, as in
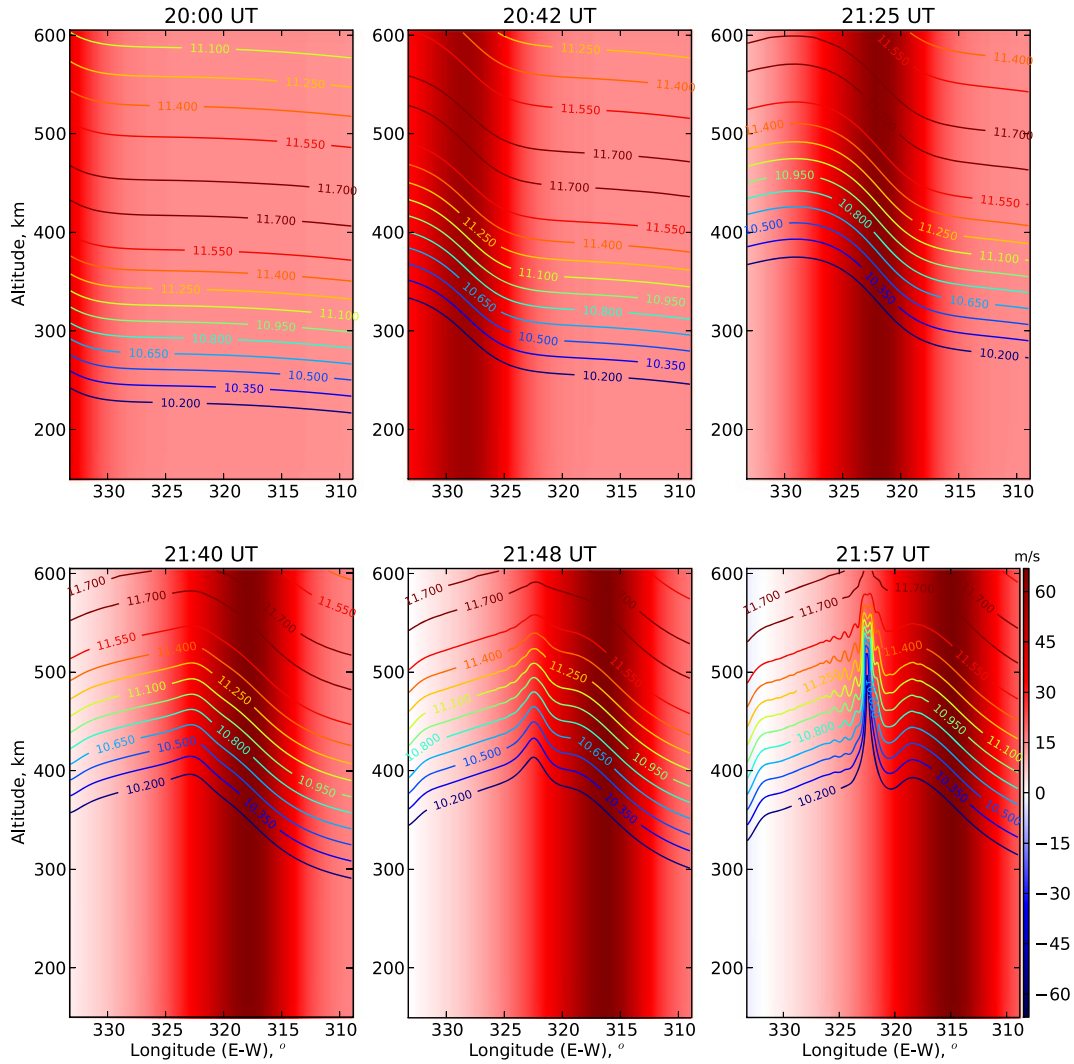
Figure 6. Evolution of the EPB represented in the form of the isodensity contours in the longitude-altitude plane under Case V: the contours of $\log_{10} n$ (represented by contours) and superimposed ambient PRVD, $u_{yt}(x, t)$ (represented by pixmap). Each panel corresponds to a chosen time which is mentioned at the top of the each panel. The colorbar represents the common scale for all pixmaps.

the present study, may act as a seeding for the CII, then the greater altitude modulated envelope, as in Figure 5b, will act more efficiently as a seeding.

[35] From 21:40 UT onward, the CII dynamics begin to dominate over PRVD dynamics and at 21:48 UT, a slight perturbation begins to develop at the longitude ($\approx 322°$) where the peak of the PRVD passed at 21:25 UT. This perturbation develops as a plasma bubble at 21:57 UT. In other words, near $322°$, a plasma bubble develops within 30 min from the time of passing of the PRVD peak at this location. Moreover, this location is 5–7° toward east of the instantaneous PRVD peak location as may be noted at $t = 21 : 57$ UT. The development of EPB within 30 min from the PRVD time suggests that the time and longitudinal-varying PRVD, as shown in Figure 5a, can efficiently seed the CII and give rise to the EPB. It may also be noted that during the development phase (21:40–21:57 UT), the EPB does not follow the movement of the PRVD or the sunset terminator, in accordance with the observations. It should be mentioned that entire region between 330 and 305° moves upward during 20:00–22:00 UT (as may be verified also from Figure 5a) and the EPB develops in this region. Thus, the EPB develops during the uplifting phase of the ionosphere and toward east of the peak of PRVD, which is also in accordance with the observations. Moreover, during the CII dominating phase, i.e., after 21:40 UT, the ionosphere begins to move downward in the longitude region eastward of $330°$ as may be verified also from Figure 5a. However, this region is 7–10° east of the region where the EPB develops and is no threat to the EPB development.

[36] It may be noted in Figure 6 that an edged density envelope is developed at $t = 21 : 40$ UT and thereafter within 30 min, this edged density modulation develops as a EPB. This aspects suggest that the formation of an edged density envelope is a crucial step leading to the development of the EPB. In this context, SAMI2 result in Figure 5b clearly shows the tendency of an edged density envelope at $t = 21 : 40$ UT. The similar behavior is noted in Figure 4 at $t = 5400$ s
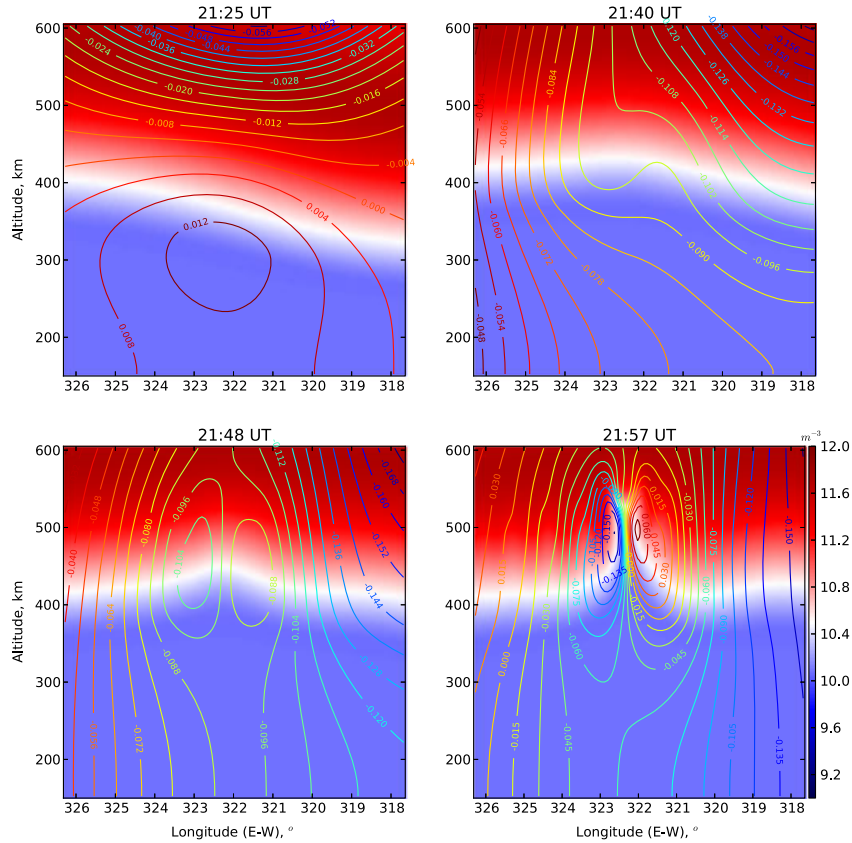
Figure 7. Evolution of the EPB represented in the form of the isodensity and the isopotential contours in the longitude-altitude plane under Case V: the contours of $\log_{10} n$ (represented by pixmap) and the contours of the normalized potential Φ/Φ_{max} (represented by contours) at few chosen time corresponding to the development phases of the CII that are mentioned at the top of the each panel. The colorbar represents the common scale for all pixmaps.

under Case IV. The PRVD with the quasi-Gaussian variation in the longitude is a common feature in both Cases IV and V. Therefore, the development of an edged density envelope and subsequent EPB in both Cases IV and V suggests that in spite other important differences between these two cases, the common ingredient, i.e., the quasi-Gaussian longitudinal variation of the PRVD, plays a decisive role in the development of an edged density envelope and subsequent development of the EPB.

[37] In Figure 7, the isodensity contours (represented by pixmap) at the time of developing phase 21:25–22:00 UT of the EPB are plotted for Case V. In these figures, the isopotential (potential Φ is normalized to the instantaneous maximum potential Φ_{max}) contours (represented by colored contours) are also superimposed. It is evident that the isopotential contours become closer in the proximity of the EPB suggesting the development of an intense polarization electric field. This polarization field is eastward in the proximity of EPB covering 321–323° longitude and outside this region toward east becomes westward. This aspect suggests that with the seeding from the PRVD of 15° longitudinal width, the EPB of $\approx 2°$ ($\sim$200-300 km) width is formed. Therefore, effect of extremely large scale seeding is to not create a huge bubble of similar size but to develop as a bubble of the longitudinal size of order of 2°. These aspects are in accordance with a conceptual sketch shown in Figure 2 of

Huang and Kelley [1996b]. It is also noted that the isopotential lines become asymmetric across the EPB owing to the sunset terminator movement.

[38] It should be noted that the PRVD configuration under Case V satisfies the threshold conditions ($v_m > 20$ m/s, $a_p > 40$ m/s) required for the development of the EPB as obtained under Case IV. Thus, these conditions are satisfied in the quiet-time ionosphere during very high solar flux period. Observations from the equatorial stations also reveal the presence of such PRVD configurations. For example, using incoherent scatter radar, *Fejer et al.* [1991] have observed very large PRVDs, up to about 80 m/s, during equinoctial periods when the solar flux was very high (F10.7 > 200). During very high solar flux summer season over São Luís, the PRVD turns out to present a quasi-Gaussian variation with the peak value of v_p >60 m/s and minimum value v_m >20 m/s [*Abdu et al.*, 2010] that satisfy the threshold conditions. It may be thus said that the longitudinally varying PRVD is capable of seeding the CII and give rise to the EPB during very high solar flux summer (over São Luís) and equinoctial (over Jicamarca) season.

[39] *Huang et al.* [2011] have recently reported the presence of wide plasma bubble during solar minimum. They also propose a new mechanism to explain the generation of these broad plasma bubbles. A series of plasma bubble starts to occur in the evening sector, and each of the

bubbles is caused by the CII. The longitudinal width of the plasma bubbles continuously grows during the rising process, so multiple bubbles with regular size can merge to form a wide bubble or a broad depletion. The upward ion drift velocity inside each individual regular bubble is driven by a polarization electric field and remains large within the wide bubble/broad depletion region. On the other hand, the mechanism simulated in the present study is applicable for very high solar flux period and it gives rise to the narrow EPB instead of broad EPB. Though, it also creates wide depletion, the electric field inside this depletion equals to the ambient electric field and not the polarization electric field. Therefore, the mechanism for broad EPB during solar minimum period as discussed by *Huang et al.* [2011] and the mechanism of broad depletion during solar maximum as simulated in the present study are of different nature and operates under different ambient conditions.

[40] The latitudinal coupling that include the off-equatorial dynamics associated with the parallel conductivity and ambipolar diffusion decelerates the evolution of EPB [*Keskinen et al.*, 2003; *Kherani et al.*, 2005; *Huba and Joyce*, 2007; *Aveiro et al.*, 2011]. These off-equatorial parallel dynamics are not considered in the present study. The decelerating effects of the off-equatorial parallel dynamics and diffusion are likely to impose more severe threshold conditions on the nature of the PRVD compared to the conditions obtained in the present study. The present study is our first attempt to simulate the seeding mechanism proposed by *Woodman* [1994] and *Huang and Kelley* [1996b] where we examine the seeding efficiency of the longitudinally varying PRVD and determine the favorable conditions for the EPB development under realistic equatorial ionospheric conditions. In the future, we plan to include the dynamics of latitudinal coupling using the three-dimensional simulation model developed by *Kherani et al.* [2005]. We also plan to include the inertia effects in our future study.

5. Summary

[41] In the present work, we examine the efficiency of the longitudinal variation of the PRVD to act as a seeding mechanism for the CII and to generate the EPB in the absence of any other kind of initial perturbation. To do so, we carried out a simulation study of the CII at the equator in a plane perpendicular to the magnetic field. At first, under few simplified cases (Cases I–IV), we examine the evolution of CII for a variety of possible PRVD configurations based on different minimum values (v_m) and amplitudes (a_p, difference between the minimum-to-peak value) that may exist in the ionosphere. In all these configurations, the longitudinal variations are chosen to be a Gaussian with 1500 km base width (full width at minimum) corresponding to 1 h time duration across the sunset terminator. Knowing the importance of v_m, a_p to determine the evolution of CII from these simplified cases, we then examine a realistic case (Case V) where the spatial-temporal configuration of the PRVD is obtained using an ambient SAMI2 model for high solar flux summer season and CII simulation is run with this realistic ambient PRVD configuration.

[42] Under the simplified Cases I–IV, to understand effects of v_m, a_p, we begin first with the various longitudinal configurations invariant in time by assuming average

PRVD=30 m/s and assuming that the sunset terminator is at a fixed location during simulation. These simulation runs are referred as Cases I–III. In the next simulation run referred as Case IV, we choose the zonal configuration corresponding to Case III and run simulation for time varying PRVD.

[43] Under Cases I–IV, it is found that the efficiency of longitudinally structured PRVD to seed the CII and to give rise to the EPB depends on the a_p and the minimum value v_m. It is found that the EPB develops only for the a_p greater than 30 m/s and for the v_m greater than 20 m/s. For $a_p = 40$ m/s and $v_m = 20$ m/s, and for time-varying PRVD, the EPB develops in 5000 s, which is approximately the time duration of PRVD in the ionosphere. This situation represents the favorable condition for the EPB development. On the other hand, for 30 m/s< a_p < 40 m/s, the EPB may develop for $v_m > 20$ m/s. However, this development occurs in 8000 s, much later than usual time duration of PRVD in the ionosphere, and thus do not represent the favorable conditions for the EPB development.

[44] The study under a realistic Case V reveals following ambient, CII, and EPB characteristics: Both PRVD and ionospheric density acquire asymmetric quasi-Gaussian envelopes with the longitudinal size $\sim 15°$ that move westward with the sunset terminator. Moreover, the realistic PRVD envelope satisfies the threshold values of v_m, a_p that are obtained under Cases I–IV. With these realistic ambient spatial-temporal PRVD, the CII simulation reveals following characteristics: Initially during 20:00–21:40 UT, the ionospheric density n acquires a quasi-Gaussian envelope in the longitude, in the form of a huge depletion, owing to the quasi-Gaussian envelope of the PRVD. This huge depletion is not a bubble since it moves with the ambient velocity. At 21:40 UT, the CII dynamics begin to dominate over PRVD and a slight perturbation begins to develop at the longitude ($\approx 322°$) where the peak of the PRVD passed at 21:25 UT. This perturbation develops into an EPB within 15 min. In other words, the EPB develops within $\sim$30 min from the time of the PRVD peak and $\approx 7°$ toward east of the instantaneous PRVD peak location as it may be noted at 21:55 UT in Figure 7. Moreover, this development utilizes effectively 2° ($\sim$ 200–300 km) scale of longitudinal variation around the peak location instead of utilizing complete scale size $\sim 15°$. It may also be noted that during the development phase (21:40–22:00) UT, the EPB does not follow the movement of the PRVD or the sunset terminator, in accordance with the observations. These evolution characteristics are found to be consistent with the proposed evolution mechanism discussed by *Huang and Kelley* [1996b].

[45] The PRVD conditions $a_p = 40$ m/s and $v_m = 20$ m/s obtained under Cases I–IV, are possible to occur during high solar flux summer season, as shown under Case V using ambient SAMI2 model. They represent the threshold conditions for the nature of PRVD that is required for the development of the EPB. These conditions are satisfied in the quiet-time ionosphere during very high solar flux. For example, during summer and very high solar flux period in the Brazilian longitude sector, the PRVD over equator often meets these conditions [*Abdu et al.*, 2010]. Very large PRVD, up to about $v_p =80$ m/s, are often observed over Jicamarca during very high solar flux equinoctial season [*Fejer et al.*, 1989]. Therefore, the seeding mechanism examined in the present study may find favorable ionospheric condition

during very high solar flux. It should also be pointed out that the PRVD threshold conditions derived from the present study are applied only to the ionospheric profile used in the simulations. It should not be indicated to be the threshold conditions for the development of EPB at high solar activity for other or arbitrary ionospheric profile. The equatorial ionospheric density profile and the peak value of the prereversal enhancement have a strong dependence on longitude and season. The threshold condition for one specific longitude is not necessarily applicable to other longitudes, and depending on the ambient conditions, the PRVD threshold conditions, obtained in the present study, may alter.

[46] The ionospheric community currently seek a better understanding of the role of seed waves in the climatology and day-to-day variability of EPBs. It is generally understood that seed waves of significant amplitude are needed for the generation of the EPBs. The seed waves would provide the initial perturbation necessary for the CII and a head start so that the timescale of simulated EPBs better match the observation of EPBs. It is, however, unclear whether or not seed waves are always present (via the acoustic-gravity wave modulation or via other plasma processes). The results of the present study suggest that at least during high solar flux conditions, seed waves are not necessary for the development of EPBs and it could be produced as a result of enhanced (and localized) PRVD seeding.

Appendix A: Derivation of the Potential Equation

[47] Using (3), the current density $\vec{J}$ can be written as follows:

$$\vec{J} = \sigma_P \vec{E} + \sigma_H \vec{E} \times b_o + b_p \frac{enB_o}{\kappa_i} \frac{\vec{g}}{v_{in}} + b_h \frac{enB_o}{\kappa_i} \frac{\vec{g}}{v_{in}} \times b_o$$

where $\sigma_{P,H}$ are the Pedersen and Hall conductivities and $b_{P,H}$ are the Pedersen and Hall mobilities. In the F region of the ionosphere, $\sigma_H << \sigma_P$ and $b_P << b_H$, leading to the following expression for the $\vec{J}$:

$$\vec{J} = \sigma_P \vec{E} + b_h \frac{enB_o}{\kappa_i} \frac{\vec{g}}{v_{in}} \times b_o; \quad \sigma_P = \frac{en}{B_o \kappa_i}; \quad b_h = \frac{1}{B_o}; \quad \kappa_i = \frac{\Omega_i}{v_{in}}$$

or

$$\vec{J} = \sigma_P \vec{E} + \sigma_P B_o \frac{\vec{g}}{v_{in}} \times b_o$$

$$\vec{J} = \sigma_P \delta E + \sigma_P \vec{E}_o + \sigma_P B_o \frac{\vec{g}}{v_{in}} \times b_o$$

$$\vec{J} = -\sigma_P \vec{\nabla} \Phi + \sigma_P B_o \vec{\Delta} u^o; \quad \delta E = -\vec{\nabla}\Phi; \quad \Delta \vec{u}^o = \vec{E}_o/B_o + \frac{\vec{g}}{v_{in}} \times b_o \quad \text{(A1)}$$

Substitution of $\vec{J}$ in (2) leads to the following equation for the potential Φ:

$$\nabla \cdot (\sigma_P \nabla \Phi) = B_o \Delta u^o \cdot \nabla \sigma_P \quad \text{(A2)}$$

In the equatorial plane, this can be expanded in the following form:

$$\frac{1}{h_\eta h_\zeta} \frac{\partial}{\partial \eta}\left(\frac{h_\eta h_\zeta}{h_\eta^2} \sigma_P \frac{\partial \Phi}{\partial \eta}\right) + \frac{1}{h_\eta h_\zeta} \frac{\partial}{\partial \zeta}\left(\frac{h_\eta h_\zeta}{h_\zeta^2} \sigma_P \frac{\partial \Phi}{\partial \zeta}\right) = B_o \Delta u^o \cdot \nabla \sigma_P$$

[48] Under a realistic case (Case V), $(\eta = \phi, \zeta = p)$ with $(h_\zeta = 1, h_\eta = r)$ are the magnetic field coordinates

at the equator, perpendicular to the Earth magnetic field where (ϕ, p) represent the longitude and altitude, respectively. Here r represents the radial distance measured from the center of the Earth. Under the simplified cases (Cases I–IV), $(\eta = x, \zeta = y)$ with $(h_\zeta = 1, h_\eta = 1)$ are Cartesian coordinates at the equator, perpendicular to the Earth's magnetic field where (x, y) represent the longitude and altitude, respectively. In the Cartesian coordinate system, above equation leads to the following potential equation [*Kherani et al.*, 2004]:

$$\nabla^2 \Phi + \frac{\partial \log(\kappa_i n)}{\partial x} \frac{\partial \Phi}{\partial x} + \frac{\partial \log(\kappa_i n)}{\partial y} \frac{\partial \Phi}{\partial y} = s;$$

$$s = -B_o\left(\frac{g}{v_{in}} + u_{yt}\right)\frac{\partial \log n}{\partial x} - B_o \frac{\partial u_{yt}}{\partial x} \quad \text{(A3)}$$

Appendix B: Numerical Method

[49] Differential equations (4) and (5) are solved using centered-space finite-difference method. For the first-order time derivative in the continuity equation (5), the forward-time difference method is adopted as follows:

$$\frac{\partial n}{\partial t} \equiv \frac{n(t + \Delta t) - n(t)}{\Delta t}; \quad \text{(B1)}$$

For the time integration of the equation (5), Crank-Nicolson implicit scheme is used so that terms other than time derivative term are estimated at $t + \Delta t$. For example, the continuity equation (5) is written as follows:

$$\frac{n^{t+\Delta t} - n^t}{\Delta t} = \nabla \cdot [n^{t+\Delta t} \cdot \vec{u}^{t+\Delta t}] \equiv \nabla \cdot F^{t+\Delta t} \quad \text{(B2)}$$

That is, the right-hand side is estimated at time $t + \Delta t$. (B2) can be rearranged as follows:

$$n(\eta, \zeta, t + \Delta t) = \theta_o n(\eta, \zeta, t) + \theta_\pm n(\eta, \zeta, \pm \Delta r, t + \Delta t) \quad \text{(B3)}$$

Here coefficients θ's are the functions of $\vec{u}(t + \Delta t)$ or $\Phi(t + \Delta t)$ which are the simultaneous solutions of equations (3)–(4).

[50] The solution, Φ, of equation (4) is obtained using centered-space finite-difference method, leading to the following difference equation:

$$\frac{\Phi^{\zeta+\Delta\zeta} - 2\Phi^\zeta + \Phi^{\zeta-\Delta\zeta}}{h_\zeta^2 \Delta\zeta^2} + \frac{\Phi^{\eta+\Delta\eta} - 2\Phi^\eta + \Phi^{\eta-\Delta\eta}}{h_\eta^2 \Delta\eta^2}$$

$$+ \Pi_\zeta^{t+\Delta t} \frac{\Phi^{\zeta+\Delta\zeta} - \Phi^{\zeta-\Delta\zeta}}{2h_\zeta\Delta\zeta} + \Pi_\eta^{t+\Delta t} \frac{\Phi^{\eta+\Delta\eta} - \Phi^{\eta-\Delta\eta}}{2h_\eta\Delta\eta} = s^{t+\Delta t}$$

$$\text{(B4)}$$

or

$$\alpha\Phi^{\zeta,\eta} = \Pi_{\zeta+\Delta\zeta}^{t+\Delta t}\Phi^{\zeta+\Delta\zeta} + \Pi_{\zeta-\Delta\zeta}^{t+\Delta t}\Phi^{\zeta-\Delta\zeta} + \Pi_{\eta+\Delta\eta}^{t+\Delta t}\Phi^{\eta+\Delta\eta}$$

$$+ \Pi_{\eta-\Delta\eta}^{t+\Delta t}\Phi^{\eta-\Delta\eta} - s^{t+\Delta t} \quad \text{(B5)}$$

Here coefficients Π's are the functions of $n(t + \Delta t)$ which is the simultaneous solution of equation (B3).

[51] Equations (B3) and (B5) lead to the set of algebraic equations for $n(\zeta, \eta, t + \Delta t)$ where each equation is obtained by changing the grid point (ζ, η). Since, in two dimension as in the present case, the number of grid points are large, (B3, B5) represent the matrix equations with large coefficient matrix. These matrix equations are solved using Successive-Over-relaxation (SOR) method.

[53] Robert Lysak thanks the reviewers for their assistance in evaluating this paper.

References

Abdu, M. A., et al. (2010), Solar flux effects on the equatorial evening vertical drift and meridional winds over Brazil: A comparison between observational data and the IRI model and the HWM representations, *Adv. Space Research*, *46*, 1078–1085.

Aveiro, H. C., D. L. Hysell, J. Park, and H. Lühr (2011), Equatorial spread F-related currents: Three-dimensional simulations and observations, *Geophys. Res. Lett.*, *38*, L21103, doi:10.1029/2011GL049586.

Balsley, B. B. (1973), Electric fields in the equatorial ionosphere: A review of techniques and measurements, *J. Atmos.Terr. Phys.*, *35*, 1035–1044.

Batista, I. S., M. A. Abdu, and J. A. Bittencourt (1986), Equatorial F region vertical plasma drifts: Seasonal and longitudinal asymmetries in the American sector, *J. Geophys. Res.*, *91*, 12,055–12,064.

Batista, I. S., R. T. deMedeiros, M. A. Abdu, J. R. deSouza, G. J. Bailey, and E. R. dePaula (1996), Equatorial ionospheric vertical plasma drift model over the Brazilian region, *J. Geophys. Res.*, *101*(A5), 10,887–10,892, doi:10.1029/95JA03833.

de Paula, E. R., E. A. Kherani, R. Y. C. Cueva, and L. A. P. Camargo (2011), Observations of pre-midnight 5-m irregularities in the equatorial F region over So Lus, Brazil: Solar flux dependence and seasonal variations, *JASTP*, *73*, 1544–1554, doi:10.1016/j.jastp.2011.03.014.

Fejer, B. G. (2012), Low latitude ionospheric electrodynamics, in *Key Processes in Solar-Terrestrial Physics*, edited by W. Gonzales and J. L. Burch, Springer, New York.

Fejer, B. G., E. R. de Paula, I. S. Batista, E. Bonelli, and R. F. Woodman (1989), Equatorial F region vertical plasma drifts during solar maxima, *J. Geophys. Res.*, *94*(A9), 12,049–12,054, doi:10.1029/JA094iA09p12049.

Fejer, B. G., E. R. de Paula, S. A. Gonzales, and R. F. Woodman (1991), Average vertical and zonal F region plasma drifts over Jicamarca, *J. Geophys. Res.*, *96*, 13,901–13,906.

Haerendel, G. R. (1973), Theory of equatorial spread F, *Unpublished report*, Max-Plank Institut fur Physik and Astrophysik, Garching, F.R.G.

Huang, C. S., M. C. Kelley, and D. L. Hysell (1993), Nonlinear Rayleigh-Taylor instabilities, atmospheric gravity waves, and equatorial spread F, *J. Geophys. Res.*, *98*, 15,631–15,642.

Huang, C. S., and M. C. Kelley (1996a), Nonlinear evolution of equatorial spread F 4. Gravity waves, velocity shear and day-to-day variability, *J. Geophys. Res.*, *101*, 24,521–24,532.

Huang, C.-S., and M. C. Kelley (1996b), Nonlinear evolution of equatorial spread F 3. Plasma bubbles generated by structured electric fields, *J. Geophys. Res.*, *101*, 303–313.

Huang, C. S., O. de La Beaujardiere, P. A. Roddy, D. E. Hunton, R. F. Pfaff, C. E. Valladares, and J. O. Ballenthin (2011), Evolution of equatorial ionospheric plasma bubbles and formation of broad plasma depletions measured by the C/NOFS satellite during deep solar minimum, *J. Geophys. Res.*, *116*, A03309, doi:10.1029/2010JA015982.

Huba, J., G. Joyce, and J. Fedder (2000), Sami2 is Another Model of the Ionosphere (SAMI2): A new low latitude ionosphere model, *J. Geophys. Res.*, *105*(A10), 23,035–23,053.

Huba, J. D., and G. Joyce (2007), Equatorial spread modeling: Multiple bifurcated structures, secondary instabilities, large density biteouts, and supersonic flows, *Geophys. Res. Lett.*, *34*, L07105, doi:10.1029/2006GL028519.

Hysell, D. L., E. Kudeki, and J. L. Chau (2005), Possible ionospheric pre-conditioning by shear flow leading to equatorial spread F, *Ann. Geophys.*, *23*, 2647–2655, http://www.ann-geophys.net/23/2647/2005/.

Keskinen, M. J., S. L. Ossakow, S. Basu, and P. J. Sultan (1998), Magnetic-flux-tube-integrated evolution of equatorial ionospheric plasma bubbles, *J. Geophys. Res.*, *103*(A3), 3957–3967, doi:10.1029/97JA02192.

Keskinen, M. J., S. L. Ossakow, and B. G. Fejer (2003), Three-dimensional non-linear evolution of equatorial ionospheric spread-F bubbles, *Geophys. Res. Lett.*, *30*(16), 1855, doi:10.1029/2003GL017418.

Keskinen, M. J. (2010), Equatorial ionospheric bubble precursor, *Geophys. Res. Lett.*, *37*, L09106, doi:10.1029/2010GL042963.

Kherani, E. A., E. R. de Paula, and F. C. P. Bertoni (2004), Effects of the fringe field of Rayleigh-Taylor instability in the equatorial E and valley regions, *J. Geophys. Res.*, *109*, A12310, doi:10.1029/2003JA010364.

Kherani, E. A., M. Mascarenhas, J. H. A. Sobral, E. R. de Paula, and F. C. Bertoni (2005), A three dimension simulation model of collisional interchange instability, *Space Sci. Rev.*, *121*, 253–269.

Kherani, E. A., M. A. Abdu, E. R. de Paula, D. C. Fritts, J. H. A. Sobral, and F. C. de Meneses Jr (2009), The impact of gravity waves rising from convection in the lower atmosphere on the generation and non-linear evolution of equatorial bubble, *Ann. Geophys.*, *27*, 1657–1668.

Kudeki, E., A. Akgiray, M. Milla, J. L. Chau, and D. L. Hysell (2008), Equatorial spread-F initiation: Post-sunset vortex, thermo- spheric winds, gravity waves, *J. Atmos. Sol. Terr. Phys.*, *69*(17–18), 2416–2427.

Ossakow, S. L., S. T. Zalesak, B. E. McDonald, and P. K. Chaturvedi (1979), Nonlinear equatorial spread F: Dependence on altitude of the F peak and bottom-side background electron density gradient scale length, *J. Geophys. Res.*, *84*, 17–29.

Raghavarao, R., R. Sekar, and R. Suhasini (1992), Nonlinear numerical simulation of equatorial spread F—Effects of winds and electric fields, *Adv. Space Res.*, *12*, 227–230.

Rodrigues, F. S., D. L. Hysell, and E. R de Paula (2008), Coherent backscatter radar imaging in Brazil: Large-scale waves in the bottomside F-region at the onset of equatorial spread F, *Ann. Geophys.*, *26*, 3355–3364, doi:10.5194/angeo-26-3355-2008.

Sekar, R., R. Suhasini, and R. Raghavarao (1994), Effects of vertical winds and electric fields in the non-linear evolution of equatorial spread F, *J. Geophys. Res.*, *99*, 2205–2213.

Sekar, R., and M. C. Kelley (1998), On the combined effects of vertical shear and zonal electric field patterns on non-linear equatorial spread F evolution, *J. Geophys. Res.*, *103*(A9), 20,735–20,747.

Sobral, J. H. A., M. A. Abdu, I. S. Batista, and C. J. Zamlutti (1980), Association between plasma bubble irregularities and airglow disturbances over Brazilian low latitudes, *Geophys. Res. Lett.*, *7*(11), 980–982.

Sultan, P. (1996), Linear theory and modeling of the Rayleigh-Taylor instability leading to the occurrence of equatorial spread F, *J. Geophys. Res.*, *101*, 26,875–26,891.

Woodman, R. F. (1994), Equatorial ionospheric irregularities as observed by the Jicamarca radar, in *Low-Latitude Ionospheric Physics*, edited by F. S. Kuo, p. 85, Pergamon Press, New York.

Woodman, R. F., and C. LaHoz (1976), Radar observations of F region equatorial irregularities, *J. Geophys. Res.*, *81*, 5447–5466

Zargham, S., and C. E. Seyler (1987), Collisional Interchange instability: Numerical simulations of intermediate-scale irregularities, *J. Geophys. Res.*, *92*, 10,073–10,088.